New Journal of Physics
The open-access journal for physics

Controlling molecular broadband-emission by optical confinement

Mathias Steiner[1,3,6], **Antonio Virgilio Failla**[1,4], **Achim Hartschuh**[1,5], **Frank Schleifenbaum**[1], **Clemens Stupperich**[2] **and Alfred Johann Meixner**[1,6]

[1] Institute of Physical and Theoretical Chemistry, Eberhard-Karls-University Tübingen, 72076 Tübingen, Germany
[2] Center for Micro- and Nanochemistry and -Engineering, Siegen University, 57068 Siegen, Germany
E-mail: msteine@us.ibm.com and alfred.meixner@uni-tuebingen.de

New Journal of Physics **10** (2008) 123017 (23pp)
Received 8 September 2008
Published 16 December 2008
Online at http://www.njp.org/
doi:10.1088/1367-2630/10/12/123017

Abstract. We investigate experimentally and theoretically the fluorescence emitted by molecular ensembles as well as spatially isolated, single molecules of an organic dye immobilized in a quasi-planar optical microresonator at room temperature. The optically excited dipole emitters couple simultaneously to on- and off-axis cavity resonances of the microresonator. The multi-spectral radiative contributions are strongly modified with respect to free (non-confined) space due to enhancement and inhibition of the molecular spontaneous emission (SpE) rate. By varying the mirror spacing of the microresonator on the nanometer-scale, the SpE rate of the cavity-confined molecules and, consequently, the spectral line width of the microresonator-controlled broadband fluorescence can be tuned by up to one order of magnitude. Stepwise reducing the optical confinement, we observe that the microresonator-controlled molecular fluorescence line shape converges towards the measured fluorescence line shape in free space. Our results are important for research on and application of broadband emitters in nano-optics and -photonics as well as microcavity-enhanced (single molecule) spectroscopy.

[3] Present address: IBM Research Division, T J Watson Research Center, Yorktown Heights, NY 10598, USA.
[4] Present address: Imaging and Microscopy Laboratory, Cambridge Research Institute of Cancer Research UK, Cambridge CB2 0RE, UK.
[5] Present address: Department of Chemistry and Biochemistry, Ludwig-Maximilians-University München, 81377 München, Germany.
[6] Author to whom any correspondence should be addressed.

Contents

1. Introduction

Optical microcavities are unique tools for controlling the radiative properties of embedded quantum mechanical emitters (QME) like atoms, ions, molecules or quantum dots, see e.g. [1]–[4] and references therein. By confining the optical field surrounding a QME on the length scale of one emission wavelength λ, the local photonic mode density (PMD) available for the spontaneous emission (SpE) of a photon can be considerably modified as compared to free, i.e. non-confined space. The SpE rate of an embedded QME is proportional to the PMD and the associated vacuum fluctuations of the optical field and can, hence, either be inhibited [5] or resonantly enhanced [6]. Since emission wavelength and emission direction are coupled for each specific cavity mode, the coupling of a broadband emitter to a cavity results in an angular redistribution of its emission with respect to free space. In the case where the emission line width of an embedded QME exceeds the spectral width of the photonic modes, we also expect that the microcavity-controlled emission is spectrally redistributed due to frequency-selective coupling efficiencies between the QME and available cavity modes. The emergence of nanophotonic devices based on individual broadband emitters in planar microresonators such as quantum dots [7], single molecules [8] or single-wall carbon nanotubes [9]–[11] as well as the recent achievement of single-molecule fluorescence control with metallic mirrors [12, 13], nanoparticles [14, 15], nanoantennas [16] or nanoapertures [17] makes it worthwhile to investigate how radiative rate alterations imposed on QMEs by optical confinement modify their emission spectrum. In particular, the applications of fluorescent molecules as single photon sources, see e.g. [18, 19] and references therein, requires experimental verification on the single molecule level.

If fluorescence studies are carried out on the single molecule level, microscopy relies on objectives having high numerical apertures, see e.g. [20]–[23] and references therein. In this

case, the complex distribution of the tightly focused laser excitation field within the cavity boundaries [24]–[27] as well as the varying detection efficiencies for on- and off-axis emissions have to be taken into account. While utilizing cavity mirrors made of metal is favorable for providing steady reflection properties as a function of both wavelength and incidence angle as well as small optical confinement volumes, the occurring phase changes and absorption further complicates the quantification [28, 29]. Experimental studies of single broadband-emitting dye molecules spatially isolated and immobilized in planar $\lambda/2$-microresonators made of silver mirrors revealed an SpE-enhancement by a factor of three as well as a sixfold narrowing of the spectral emission linewidth with respect to free (non-confined) space [30]. However, the occurring modifications of spectral line shapes have not been linked to the microresonator-controlled SpE-rate so far.

In this paper, we correlate the SpE rate and the fluorescence spectrum of broadband-emitting dye molecules embedded in a planar $\lambda/2$-microresonator under controlled variation of the mirror spacing. In a first step, we use the first-order perturbation theory to calculate the microresonator-controlled SpE-rate that has been measured for both molecular ensembles and single molecules using time-resolved spectroscopy. Based on these results, in a second step, we model the measured line shape of the spectrally dispersed fluorescence emission collected with high numerical apertures as function of the mirror spacing. In the calculations, we sum on- and off-axis radiative contributions undergoing different numbers of internal reflections in the planar microresonator and find good agreement with the experimental results by accounting for the complex interplay between the molecular fluorescence properties, the focused pump field, the optical properties of the microresonator and the detection conditions. Stepwise increasing the mirror spacing from $\lambda/2$ to 10λ, we observe that the microresonator-controlled fluorescence spectrum approaches the spectral distribution measured in free space demonstrating the gradual decrease of the optical confinement imposed by the metal mirrors.

2. Experimental section

Figure 1(a) shows a schematic of the optical setup and the microresonator configuration. We prepared the resonator mirrors $M_{1,2}$ by evaporating silver films onto glass microscope cover slips. A thin layer of a transparent adhesive (NOA 61, Norland) doped with uniformly distributed and randomly oriented perylene-type molecules (N-(2,6-diisopropylphenyl)-perylen-3,4-dicarboxymide, abbreviated PI, for structural formula see figure 1(b)) in two different concentrations separates the two mirrors: the higher dopant concentration $c_{\mathrm{PI}} = 10^{-5}\,\mathrm{mol\,l^{-1}}$ results in an average intermolecular distance of $\delta_{\mathrm{PI}} = 50\,\mathrm{nm}$ in the intra-cavity medium, the lower concentration $c_{\mathrm{PI}} = 10^{-10}\,\mathrm{mol\,l^{-1}}$ corresponds to an average intermolecular distance $\delta_{\mathrm{PI}} = 2000\,\mathrm{nm}$. The measured fluorescence spectrum $f_{\mathrm{n}}(\lambda)$ of an ensemble of PI molecules immobilized in a thin film of the intra-cavity medium but without optical confinement due to metal mirrors is shown in figure 1(b) and serves as a reference in the following. During the manufacturing process and the curing of the intra-cavity medium, we apply a punctual force to one of the resonator mirrors in order to introduce a slight curvature across the microresonator sample. This curvature can be approximated by assuming that the two mirrors exhibit a local tilt α in the range of 10^{-3}–10^{-2} resulting in a gradual variation of the mirror spacing L across the (x, y)-plane as indicated schematically in figure 1(a). The wide-field transmission microscope image shown in figure 1(c) exhibits a part of the dark center of the microresonator corresponding to mirror spacings smaller than one half wavelength in the

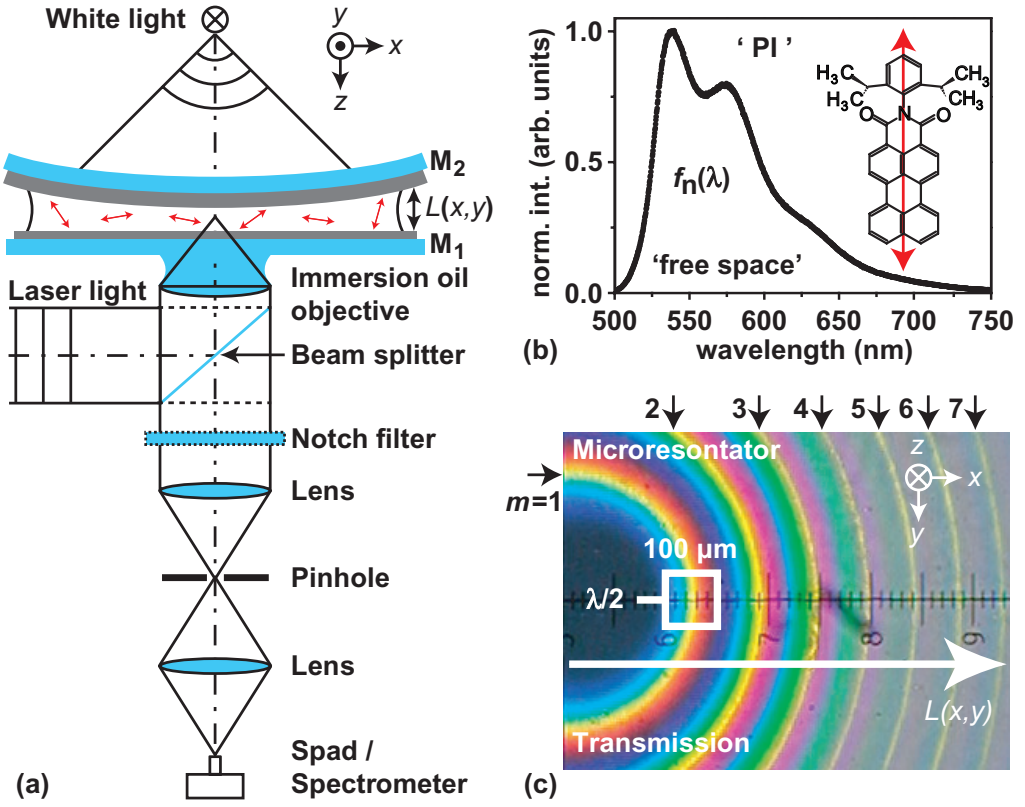

Figure 1. (a) Schematic of the experimental setup and the microresonator consisting of two silver mirrors $M_{1,2}$ on glass substrates separated by a thin polymer layer that is doped with spatially immobilized molecular dipole emitters indicated by double arrows (spad: single-photon avalanche diode). (b) Normalized free-space (non-confined) fluorescence spectrum $f_n(\lambda)$ of an ensemble of PI molecules embedded in the transparent intra-cavity medium. In the structural formula of PI, the orientation of the molecular transition dipole is indicated by a double arrow. (c) Optical transmission micrograph of the microresonator illuminated simultaneously with white light and laser light ($\lambda_{laser} = 570$ nm). The transmission maxima for the laser light are marked by arrows to indicate the different orders of interference m.

visible spectral range. The transmission minimum is enclosed by the $\lambda/2$-regime, i.e. the first order of interference $m = 1$, and with increasing distance from the center we observe concentric circles (Newton rings) formed by the transmission maxima corresponding to larger m-values. Locally, on the micrometer scale, the sample acts as a planar resonator in a good approximation yielding a cavity-Q around 50 throughout the $\lambda/2$-regime. Details regarding manufacturing and characterization of the microresonator as well as its implication on single molecule spectroscopy have already been reported [30]–[32]. For every (x, y)-position, the mirror spacing $L(x, y)$ is calculated from the maximum local transmission wavelength $\lambda(x, y)$ following [28, 33] by using

$$L(x, y) = \left(m - \frac{\sum_i \Delta\phi_i \, (d_i, \vartheta, \lambda)}{2\pi} \right) \frac{\lambda(x, y)}{2 n_{pol} \cos\vartheta}. \quad (1)$$

Here, m denotes the order of interference, $\Delta\phi_i$ the phase change due to reflection at the respective silver mirror $i = 1, 2$ with thickness d_i, $n_{\mathrm{pol}} = 1.56$ the refractive index of the cured polymer and ϑ the angle of incidence (with respect to the mirror normal) of an incoming light beam with wavelength λ. Throughout the paper, we will refer to the case $d_1 = 30\,\mathrm{nm}$ and $d_2 = 60\,\mathrm{nm}$ and the corresponding mirror reflectivities R_i (for example $R_1 = 0.7$, $R_2 = 0.9$ assuming $\lambda = 532\,\mathrm{nm}$, $\vartheta = 0$) used in this work have been calculated as functions of d_i, ϑ and λ by accounting for the positions of each specific silver layer in the actual microresonator configuration (for details see section 3.1). Experimentally, $\lambda(x, y)$ is extracted from the local on-axis transmission spectrum of the microresonator as measured by illuminating the sample from the top (see figure 1(a), ϑ=0) and using a confocal pinhole having a diameter of 100 μm. The resulting L-calibration for each sample position can be reproduced with an accuracy of $\Delta L = \pm 3\,\mathrm{nm}$. For a given $\lambda(x, y)$, the occurring phase changes $\sum_i \Delta\phi_i$ ($\simeq 1.85$ as calculated for the actual configuration) reduce L by around 50 nm as compared to the case of ideal metal mirrors, i.e. neglecting absorption in the silver layers.

We use scanning confocal fluorescence microscopy to study locally the emission properties of the different microresonator samples. An immersion oil microscope objective (100x, numerical aperture NA = 1.3) tightly focuses either a pulsed or a continuous linearly polarized laser beam ($\lambda_{\mathrm{laser}} = 488\,\mathrm{nm}$) through mirror M_1 and also collects the molecular fluorescence emission (see figure 1(a)). We spatially address different sample positions (x, y) and, hence, mirror spacings $L(x, y)$ by horizontally moving the microresonator sample with respect to the fixed microscope objective using a scanning stage with nanometer accuracy. We perform time-resolved fluorescence spectroscopy based on time-correlated single photon counting and acquire steady-state fluorescence spectra using grating spectroscopy. A more detailed discussion of the experimental setup and methods can be found in [30].

3. Computational section

In the following, we outline how to model the spectral line shape of the microresonator-controlled broadband emission in four steps: firstly, we implement the coefficients that determine reflection, transmission and absorption properties of the microresonator mirrors. Secondly, we calculate the microresonator-controlled molecular SpE rate based on the optical properties of the actual microresonator mirrors and the dopant molecules embedded in the intra-cavity medium. Thirdly, we quantify the collection efficiencies for on- and off-axis emissions that are determined by the geometries of both the microresonator and the detection system. Fourthly, we scale the molecular absorption to the strength of the tightly focused laser excitation field that is strongly modified with respect to non-confined space due to the presence of the metal boundaries.

3.1. Microresonator mirrors

We calculate the reflection coefficients r_i and transmission coefficients t_i of the microresonator mirrors M_i with $i = 1, 2$ as functions of ϑ and λ by virtually propagating light beams through the actual microresonator configuration as sketched in figure 2(a). The optical properties of the absorbing silver layers (index s) with thickness d_i have been implemented based on the dielectric function of silver [28, 33]. The different transparent media, i.e. the intra-cavity polymer (index p) and the mirror substrates made of glass (index g), have been implemented

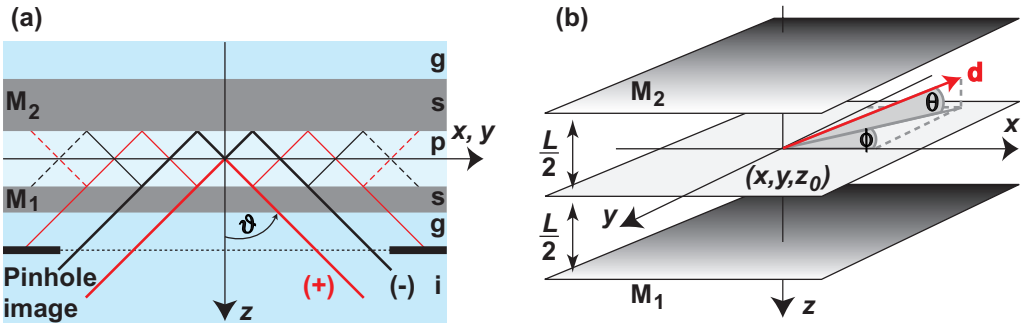

Figure 2. (a) Microresonator schematic indicating the optical multi-layer structure (g: glass, s: silver, p: polymer, i: immersion oil) for modeling the reflection and transmission coefficients of the cavity mirrors $M_{1,2}$ as well as the detectable microresonator-controlled emission consisting of contributions (+) and (−). The image of the confocal pinhole (see also figure 1(a)) is located on M_1 and determines the effective observation area on the microresonator surface. Here, it is plotted at the glass–oil interface (horizontal dashed line) for convenience. (b) Coordinate system indicating the orientation of the molecular transition dipole **d** located at the center z_0 between the cavity mirrors $M_{1,2}$.

based on their refractive indices and we can write

$$r_i(d_i, \vartheta, \lambda) = \frac{r_{gs}(d_i, \vartheta, \lambda) + r_{sp}(d_i, \vartheta, \lambda) \exp[i2\beta]}{1 + r_{gs}(d_i, \vartheta, \lambda) r_{sp}(d_i, \vartheta, \lambda) \exp[i2\beta]}, \tag{2}$$

$$t_i(d_i, \vartheta, \lambda) = \frac{t_{gs}(d_i, \vartheta, \lambda) t_{sp}(d_i, \vartheta, \lambda) \exp[i\beta]}{1 + r_{gs}(\vartheta, \lambda) r_{sp}(d_i, \vartheta, \lambda) \exp[i2\beta]}, \tag{3}$$

where the pairs of indices (gs) and (sp) label the reflection and transmission coefficients obtained at each individual dielectric–silver interface. The phase term

$$\beta = \frac{2\pi}{\lambda} n_s(\lambda) \cos(\vartheta_s), \tag{4}$$

contains the index of refraction of silver, n_s, and a complex quantity $\cos(\vartheta_s)$ that is obtained by applying Snell's law to the respective dielectric-silver interface.

3.2. The microresonator-controlled SpE rate

Theoretical approaches of the microresonator-controlled SpE rate Γ_{SpE} account for either (A) the modified intra-cavity field $\mathbf{E}_{cav}(\mathbf{k}, L)$ or (B) the modified PMD $\rho_{cav}(\mathbf{k}, L)$ inside the planar microresonator. The alternative approaches by Björk and Yamamoto (A) as well as Brorson (B) reported in [1] lead to the same conclusions and are in agreement with the results obtained based on the quantum theoretical treatment presented by De Martini *et al* in [34]. In the following, we outline an extension of approach (A) suited for broadband dipole emitters in planar microresonators made of two (absorbing) metal mirrors having different thickness.

Starting from Fermi's golden rule [35], we write the microresonator-controlled SpE rate Γ_{SpE} at wave vector $\mathbf{k}$ with $|\mathbf{k}| = k = 2\pi/\lambda = \omega/c$ as

$$\Gamma_{\mathrm{SpE}} = \frac{2\pi}{\hbar^2 c} \sum_{\mathbf{k}} |\langle |\mathbf{d} \cdot \mathbf{E}_{\mathrm{cav}}(\mathbf{k}, L)| \rangle|^2 \rho_{\mathrm{cav}}(\mathbf{k}, L), \tag{5}$$

where $\mathbf{d}$ denotes the transition dipole moment of an embedded molecule. The orientation of $\mathbf{d}$ with respect to the Cartesian coordinate system of the microresonator having its origin at z_0 in the center between the resonator mirrors $\mathrm{M}_{1,2}$ is given by the azimuthal and polar angle θ and ϕ, respectively (see figure 2(b)). For convenience, however, we calculate the molecular SpE rate Γ_{SpE} as a function of the angle ϑ enclosed by $\mathbf{k}$ and the z-axis, while we use the notation θ in the discussion to highlight the rate effects associated with the tilt angle between the molecular transition dipole and the resonator mirrors $\mathrm{M}_{1,2}$.

The intra-cavity field $\mathbf{E}_{\mathrm{cav}}(\mathbf{k}, L)$ is represented by a superposition of two sets of counter-propagating plane waves, i.e.

$$\mathbf{E}_{1,+} = \frac{t_1 \exp\left[\mathrm{i}(2\pi/\lambda)(L + z_0)\cos\vartheta\right]}{1 - r_1 r_2 \exp\left[\mathrm{i}(4\pi/\lambda)L\cos\vartheta\right]} \mathbf{E}_0, \tag{6}$$

$$\mathbf{E}_{1,-} = \frac{t_1 r_2 \exp\left[\mathrm{i}(2\pi/\lambda)(L - z_0)\cos\vartheta\right]}{1 - r_1 r_2 \exp\left[\mathrm{i}(4\pi/\lambda)L\cos\vartheta\right]} \mathbf{E}_0 \tag{7}$$

and

$$\mathbf{E}_{2,-} = \frac{t_2 \exp\left[\mathrm{i}(2\pi/\lambda)(L - z_0)\cos\vartheta\right]}{1 - r_1 r_2 \exp\left[\mathrm{i}(4\pi/\lambda)L\cos\vartheta\right]} \mathbf{E}_0, \tag{8}$$

$$\mathbf{E}_{2,+} = \frac{t_2 r_1 \exp\left[\mathrm{i}(2\pi/\lambda)(L + z_0)\cos\vartheta\right]}{1 - r_1 r_2 \exp\left[\mathrm{i}(4\pi/\lambda)L\cos\vartheta\right]} \mathbf{E}_0, \tag{9}$$

assuming a zero-point field fluctuation $\mathbf{E}_0$ impinging on either the lower mirror M_1 or the upper mirror M_2. The field reflection and transmission coefficients r_i and t_i of the microresonator mirrors M_i with $i = 1, 2$ are given by (2) and (3).

We express the s-polarized emission by decomposing the intra-cavity field in one component $\mathbf{E}_{\parallel}$ that is polarized parallel to the mirror plane and one component $\mathbf{E}_z$ that is polarized along the optical axis z:

$$\mathbf{E}^2_{\mathrm{s},\parallel} = \frac{|\mathbf{E}_{1,+} + \mathbf{E}_{1,-}|^2 + |\mathbf{E}_{2,-} + \mathbf{E}_{2,+}|^2}{2}, \tag{10}$$

$$\mathbf{E}^2_{\mathrm{s},z} = 0. \tag{11}$$

In case of p-polarized emission, we get

$$\mathbf{E}^2_{\mathrm{p},\parallel} = \frac{|\mathbf{E}_{1,+} + \mathbf{E}_{1,-}|^2 + |\mathbf{E}_{2,-} + \mathbf{E}_{2,+}|^2}{2} \cos^2\vartheta, \tag{12}$$

$$\mathbf{E}^2_{\mathrm{p},z} = \frac{|\mathbf{E}_{1,+} - \mathbf{E}_{1,-}|^2 + |\mathbf{E}_{2,-} - \mathbf{E}_{2,+}|^2}{2} \sin^2\vartheta. \tag{13}$$

The p-polarized emission has its field component in the plane defined by $\mathbf{k}$ and the z-axis whereas the s-polarized emission has its field component normal to that plane.

We calculate the microresonator-controlled SpE rate for a molecular transition dipole located at z_0 and oriented parallel to the cavity mirrors in the y-direction (see figure 2(b)) by using

$$\Gamma_{\mathrm{SpE},y}(\lambda, L) = \frac{3\Gamma_{\mathrm{SpE},0}}{4\pi} \int_0^{2\pi} \mathrm{d}\phi \int_0^{\pi/2} \sin\vartheta \,\mathrm{d}\vartheta \mathbf{E}_{\parallel}^2 D(\vartheta, \phi) f_{\mathrm{n}}(\lambda) \tag{14}$$

with $\mathbf{E}_{\parallel}^2 = \mathbf{E}_{\mathrm{s},\parallel}^2 + \mathbf{E}_{\mathrm{p},\parallel}^2$ and $D(\vartheta, \phi) = \cos^2\phi + \sin^2\phi\cos^2\vartheta$. To account for the broadband fluorescence of PI molecules, we weight the rates $\Gamma_{\mathrm{SpE},j}(\lambda, L)$ by the wavelength-dependent oscillator strength of the radiative transition that is derived from the measured and normalized free-space fluorescence spectrum $f_{\mathrm{n}}(\lambda)$ of PI molecules embedded in the intra-cavity medium but in absence of the silver mirrors (see figure 1(b)). In order to obtain absolute SpE rates, we have to scale the $\Gamma_{\mathrm{SpE},j}(\lambda, L)$-values with respect to the measured molecular SpE rate in free (non-confined) space $\Gamma_{\mathrm{SpE},0}$ using

$$\Gamma_{\mathrm{SpE},0} = \Gamma_{\mathrm{meas},0} - \Gamma_{\mathrm{nr}} = \Gamma_{\mathrm{meas},0} - (1 - Y_0)\Gamma_{\mathrm{meas},0} \tag{15}$$

where $\Gamma_{\mathrm{meas},0} = (\tau_{\mathrm{meas},0})^{-1} = (4.2 \times 10^{-9}\,\mathrm{s})^{-1}$ is the free-space excited state (fluorescence) decay rate and Y_0=0.75 the molecular fluorescence quantum yield, respectively, measured for PI molecules embedded in the intra-cavity polymer in absence of the silver mirrors [30]. The non-radiative molecular excited state decay rate Γ_{nr} is dominated by intra-molecular dynamics and cannot be modified by variations of the PMD as imposed by the microresonator. However, plasmonic coupling results in a non-radiative transfer of the molecular-excited state energy from the molecules to the metal mirrors, a process that becomes very efficient for molecule–metal distances in the range of several nanometers, see e.g. [29]. This effect combined with inefficient molecular excitation conditions close to the metal mirrors effectively prevents experimental observation of molecules displaced by more than a few tens of nanometer from the resonator center z_0.

3.3. Detectable microresonator-controlled emission

Following the procedure outlined in the previous section, we calculate for each mirror spacing L the microresonator-controlled SpE rates $\Gamma_{\mathrm{SpE},j}$ as a function of ϑ and λ assuming a single molecular dipole emitter to be located in the center z_0 of the microresonator and oriented in $j = x, y, z$ direction (see figure 2(b)). We then weight the sum of radiative rates for the three dipole orientations $\sum_j \Gamma_{\mathrm{SpE},j}(\lambda, L) f_{\mathrm{n}}(\lambda)$ using the Fabry–Perot theory [33]. In order to obtain the radiation contributions that reach the detector, we decompose the microresonator-controlled emission that pass the (in-/out-coupling) mirror M_1: the first contribution (+) comprises the emissions directed towards M_1, the second contribution (−) contains the emissions directed towards M_2 (see figure 2(a)). We calculate the transmission coefficients t_+ and t_- for both s- and p-polarized emission for the case $\vartheta = 0$ and we get

$$t_+ = \frac{t_1 \exp[0.5\mathrm{i}kL\cos\vartheta]}{1 - A}, \tag{16}$$

$$t_- = \frac{r_2 t_1 \exp[1.5\mathrm{i}kL\cos\vartheta]}{1 - A}, \tag{17}$$

while in case $\vartheta \neq 0$ we obtain

$$t_+ = \frac{t_1 \exp[0.5ikL\cos\vartheta](1 - A^{(N_+ + 1)})}{1 - A}, \tag{18}$$

$$t_- = \frac{r_2 t_1 \exp[1.5ikL\cos\vartheta](1 - A^{(N_- + 1)})}{1 - A}. \tag{19}$$

In (16) to (19), we introduced the following abbreviations

$$A = r_1 r_2 \exp(2ikL\cos\vartheta), \tag{20}$$

$$N_+ = \frac{\tan\vartheta_{\max}}{\tan\vartheta} - 0.25, \tag{21}$$

$$N_- = \frac{\tan\vartheta_{\max}}{\tan\vartheta} - 0.75; \tag{22}$$

where the maximum collection angle $\vartheta_{\max}$ is related to the numerical aperture NA of the microscope objective by $\mathrm{NA} = n_g \sin(2\vartheta_{\max})$, while N_+ and N_- account for the number of intracavity roundtrips of the microresonator-controlled emissions. The transmission function of the microresonator T_{cav} can now be written as

$$T_{\mathrm{cav}}(\lambda, \vartheta, L) = \left(|t_+|^2 + |t_-|^2\right) \frac{\cos\vartheta}{\cos\vartheta'}, \tag{23}$$

where ϑ and ϑ' are connected via Snell's law. We define the transmission function of the microscope objective T_{obj} by

$$T_{\mathrm{obj}}(\lambda, \vartheta, L) = 1 \quad (\vartheta \leqslant \vartheta_{\max}), \tag{24}$$

$$T_{\mathrm{obj}}(\lambda, \vartheta, L) = 0 \quad (\vartheta > \vartheta_{\max}). \tag{25}$$

Finally, the detected microresonator-controlled emission for a molecule located in the center z_0 of the microresonator and oriented parallel to $\mathrm{M}_{1,2}$ is given by

$$\Gamma^{\mathrm{det}}_{\mathrm{SpE},y}(\lambda, L) = \frac{3\Gamma_{\mathrm{SpE},0}}{4\pi} \int_0^{2\pi} \mathrm{d}\phi \int_0^{\pi/2} \sin\vartheta \,\mathrm{d}\vartheta \, \mathbf{E}_{\parallel}^2 D(\vartheta, \phi) f_{\mathrm{n}}(\lambda) T_{\mathrm{obj}} T_{\mathrm{cav}}. \tag{26}$$

In a last step, we introduce the pinhole (spatial filter) that is placed in the detection path of the confocal microscope (see figure 1(a)) by accounting for the pinhole image on the microresonator surface as sketched in figure 2(a). The maximum collection angle $\vartheta_{\max}$ is either limited by the NA of the microscope objective or by the effective observation diameter p on M_1, depending on ϑ and L. The reason is that off-axis emissions propagate along the mirror surfaces in the (x, y)-plane of the microresonator due to multiple internal reflections (see figure 2(a)). As a result, the detection efficiency for off-axis emissions decreases with decreasing pinhole diameter. In the present case, the diameter of the pinhole image p, or, in other words, the effective observation area on the microresonator mirror M_1, is given by the actual pinhole diameter (100 μm and 200 μm, respectively) divided by the magnification of the microscope objective (100×).

3.4. Microresonator-controlled excitation field

The efficiency of molecular excitation strongly depends on the optical field distribution inside the microresonator. Therefore, the calculated spectra are scaled by the strength of the linearly polarized and tightly focused laser excitation field at the microresonator center z_0=0 as a function of L (see figure 2(b)). The resulting values $\mathbf{E}_0(L)$ enter (6) to (9). Details of how the presence of the silver mirrors affect the focused laser excitation field and methods for quantification of the occurring effects have already been reported [27].

4. Results and discussion

4.1. Microresonator-controlled fluorescence rate

In the following, we compare the experimental results obtained for two different concentrations of fluorescent dopant molecules in the intra-cavity medium. The schematics in figures 3(a) and (b) indicate how a low-dopant concentration in the intra-cavity medium enables spatially addressing single molecules in the microresonator with the confocal microscope while for a high dopant concentration individual molecules cannot be spatially resolved. We acquired the fluorescence intensity images shown in figures 3(c) and (d) by (x,y)-scanning the microresonator samples with respect to the optical axis of the confocal microscope (see figure 1(a)). In the following, we refer to the microresonator position by the x-coordinate only. The integrated fluorescence intensity cross sections taken along the white dashed lines in the scan images are shown in figure 3(e) and (f). For single molecule doping, the fluorescence intensity scan (see figure 3(e)) exhibits fluorescence intensity peaks for several (x)-positions and, hence, mirror spacings $L(x)$ where single molecule fluorescence is on resonance with the microresonator. The gray background indicates the L-regime where single molecule fluorescence was above the detection limit of the experimental setup. High-resolution scan images as well as single photon emission characteristics (photon-antibunching) of the microresonator-controlled single molecule fluorescence have already been reported [8]. For high molecular dopant concentration, the integrated intensity cross section (see figure 3(f)) is a smooth curve having its maximum at a position x where the local resonance wavelength of the microresonator $\lambda(x)$ overlaps well with the free space fluorescence spectrum of the dye $f_n(\lambda)$ that is shown in figure 1(b).

We now address systematically different (x)-positions in both samples and analyze the extracted fluorescence emissions using time-resolved spectroscopy. In figure 4, we show typical experimental fluorescence decays for single molecules as well as molecular ensembles acquired for different mirror spacings L. We fitted single exponential model functions convoluted with the measured instrument response function (see figure 4(d)) having a full-width-at-half-maximum-value around 500 ps to the experimental decay curves. From the fit results, we obtain the experimental rates $\Gamma_{SpE}(L)$ by subtracting the non-radiative decay contributions by using

$$\Gamma_{SpE}(L) = \Gamma_{meas}(L) - \Gamma_{nr} = \frac{1}{\tau_{meas}(L)} - \frac{(1 - Y_0)}{\tau_{meas,0}}. \tag{27}$$

The experimental results are shown in figure 5 together with the results of our numerical calculations. We used the procedure outlined in section 3.2 to calculate $\Gamma_{SpE}(L) = \int \Gamma_{SpE}(\lambda, L)\, d\lambda$ assuming single PI molecules located in the center of the microresonator for two different transition dipole orientations $\theta = 0^\circ$ and 40°, respectively (see also figures 2(b) and 3(a)).

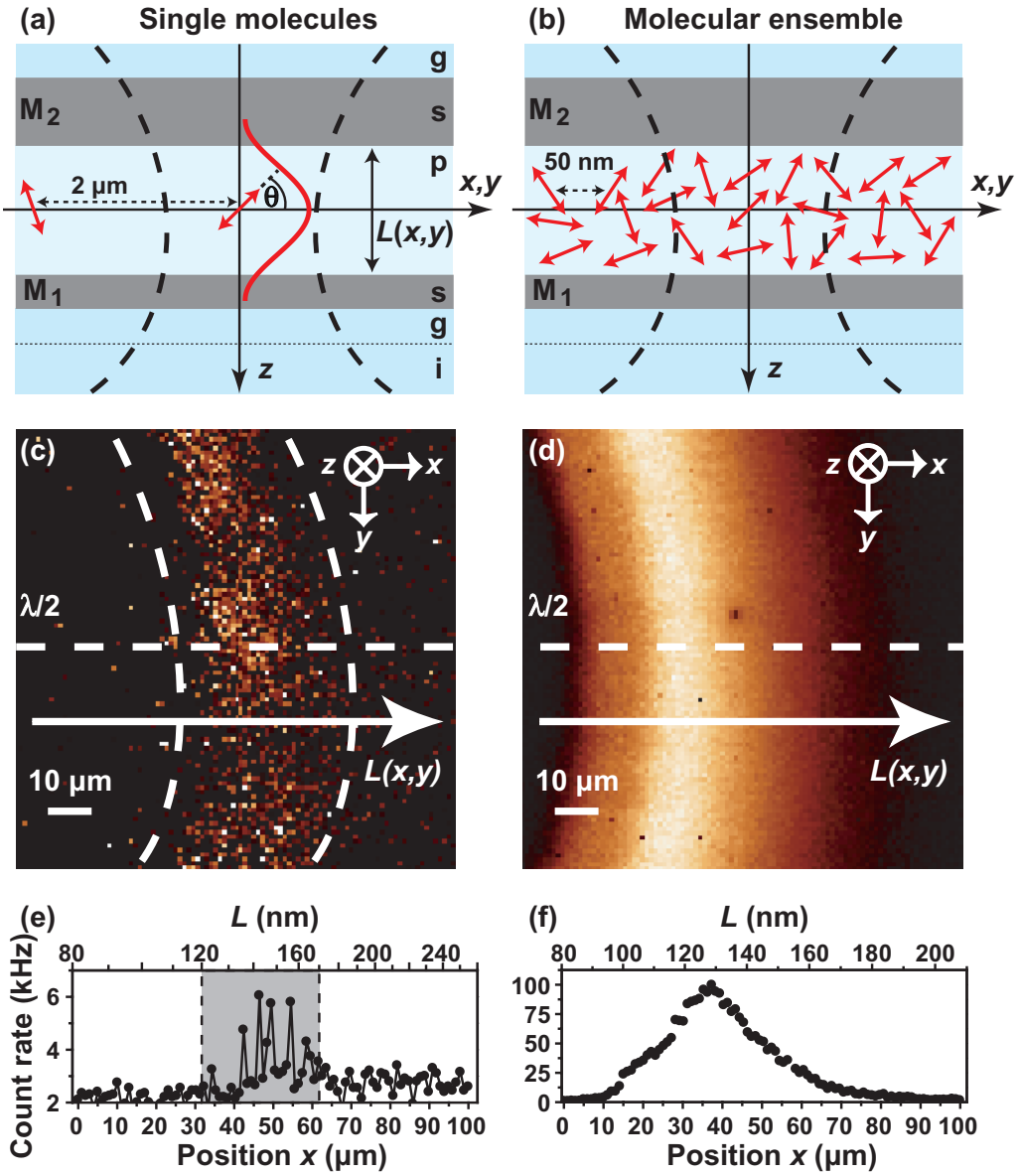

Figure 3. (a) and (b) Schematics of the microresonator structure (g: glass, s: silver, p: polymer, i: immersion oil) indicating the spatial intensity profile of the on-axis cavity resonance as well as the lateral extension of the focused laser field (dashed lines). (c) and (d) Confocal fluorescence intensity images of a section of the $\lambda/2$-regime (corresponding to the white frame in figure 1(c)) for two samples having intermolecular distances that are larger (a) or smaller (b) than the focal diameter. (e) and (f) Spectrally integrated microresonator-controlled fluorescence intensity measured along the dashed horizontal lines in images (c) and (d), respectively. The gray area in (e) marks the *L*-regime where the fluorescence signal of single PI molecules was above the experimental detection limit.

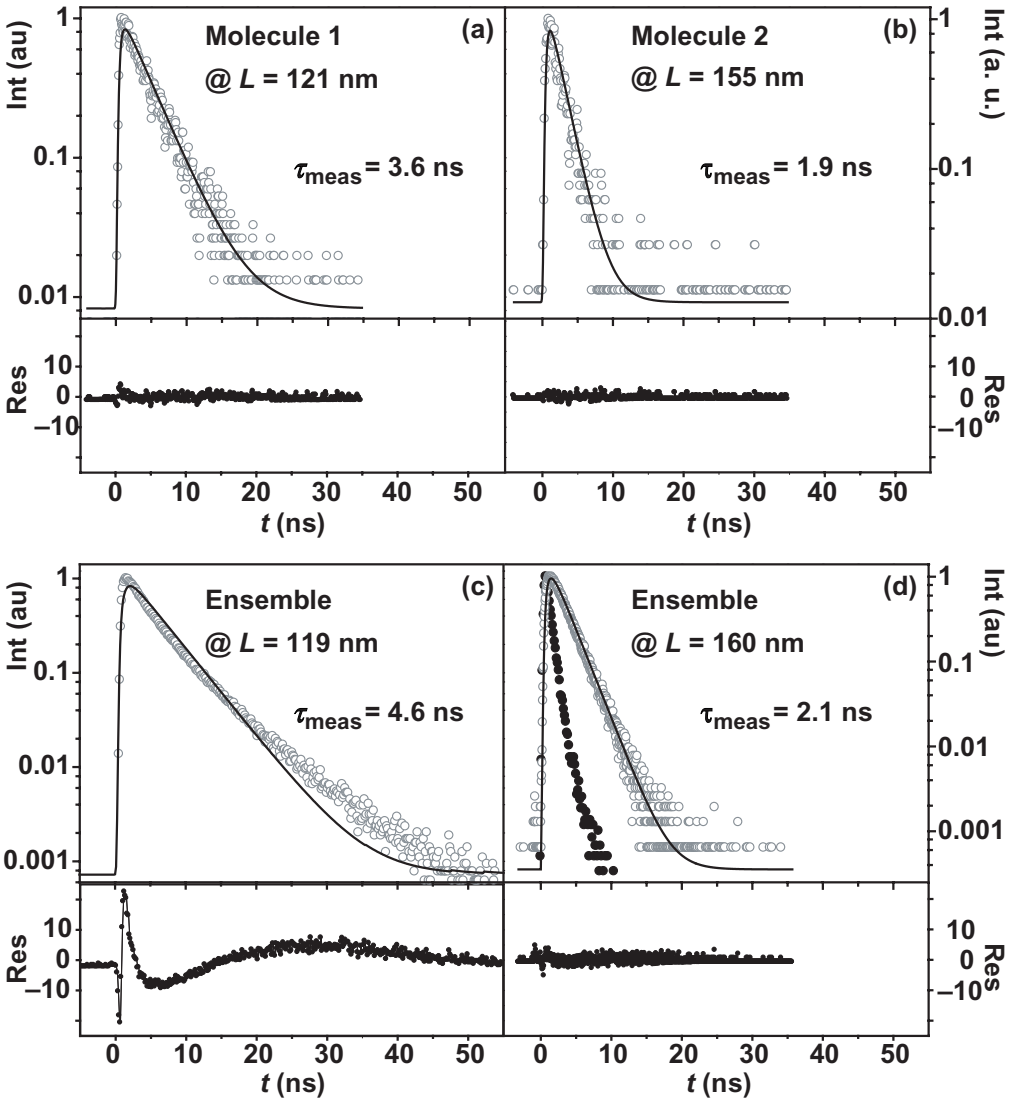

Figure 4. Measured (rings) and fitted (lines) microresonator-controlled fluorescence decays for single molecules (a) and (b), and molecular ensembles (c) and (d) at representative mirror spacings L. The residuals below show deviations between measured decays and single exponential model functions convoluted with the instrument response function (dots in (d)).

Spatially isolated, single molecules show mono-exponential decay curves (see figures 4(a) and (b), the respective signal-to-noise ratios are 15 and 7) and Γ_{SpE}-values that vary with the mirror spacing [30]. As shown in figure 5, different molecules can have different SpE-rates for the same L reflecting a strong dependence on the angle θ between the transition dipole moment and the mirror planes of the microresonator as well as a displacement of molecules from the microresonator center. A comparison of the $\Gamma_{\mathrm{SpE}}(L)$-values derived from the fits shown in figures 4(a) and (b) with the theoretical curves indicate that both molecules 1 and 2 are located in the center of the microresonator and are oriented parallel to the mirror planes (i.e. $\theta = 0^{\circ}$ in figures 2(b) and 3(a)) matching the respective maximum theoretical $\Gamma_{\mathrm{SpE}}(L)$-value.

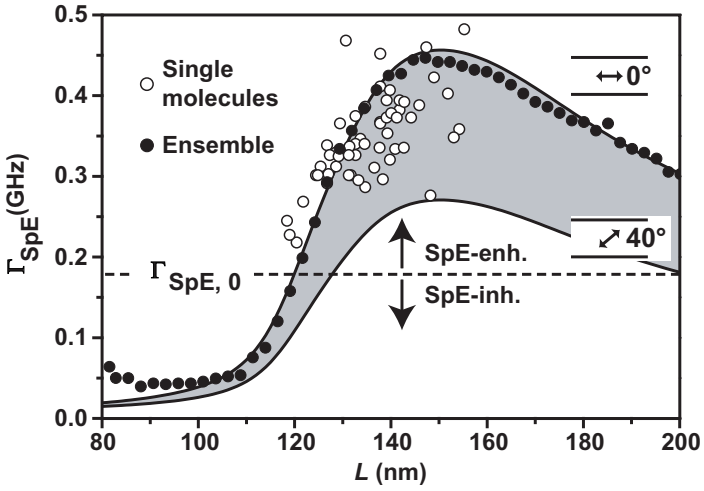

Figure 5. Microresonator-controlled SpE-rates derived from measured fluorescence decays (see figure 4) for single, spatially isolated PI molecules (rings) and PI ensembles (circles). Calculated SpE-rates (lines) for PI molecules centered in the microresonator and having their transition dipole tilted with respect to the mirror planes by 0° and 40°, respectively (see also figure 2(b)). The curve assuming a molecular tilt of 40° also represents the SpE-rate of a PI molecule oriented parallel to the cavity mirrors but displaced from the cavity center by $\Delta z = \pm 30$ nm.

Variation of the mirror spacing results in a SpE-rate modulation due to SpE-enhancement [6] and -inhibition [5], respectively. Even though molecules having transition dipole moments with $\theta \neq 0°$ are excited in our experiment, the fluorescence decays of molecular ensembles are obviously determined by molecules having $\theta = 0°$ that offer the fastest radiative decay rates. Considering the molecular ensemble as a superposition of non-interacting molecules, we would expect multi-exponential decay dynamics for all mirror spacings. More specifically, the measured ensemble decay curves (see figures 4(c) and (d)) would result from a sum of mono-exponential decay functions reflecting the orientation and spatial position of each molecule (see figure 5). Our experimental results therefore indicate an efficient coupling mechanism of excited molecules mediated by the microresonator. To determine the contribution of fluorescence resonance energy transfer (FRET), we compare the Förster radius of PI molecules with their average distance in the sample. We find that the free-space Förster radius of 1 nm is far smaller than the average molecular distance $\delta_{PI} = 50$ nm. Hence, the distance-dependence of FRET scaling with r^{-6} is not sufficient to explain intermolecular coupling, even accounting for the measured radiative rate enhancement of up to 2.5. On the other hand, we observe the resonator-mediated long-range coupling also through the formation of spatial modes having diameters of hundreds of nanometers [36]. In the literature, several concepts for resonator-mediated coupling have been presented [37]–[43]. However, as we will demonstrate in the following sections, the differences in the fluorescence decay dynamics of single molecules and molecular ensembles as observed in our experiments do not result in significant spectral effects.

As the main result of our time-resolved measurements we observe that the SpE rate of PI molecules can be inhibited (enhanced) by a factor of 0.21 (2.5) with respect to the

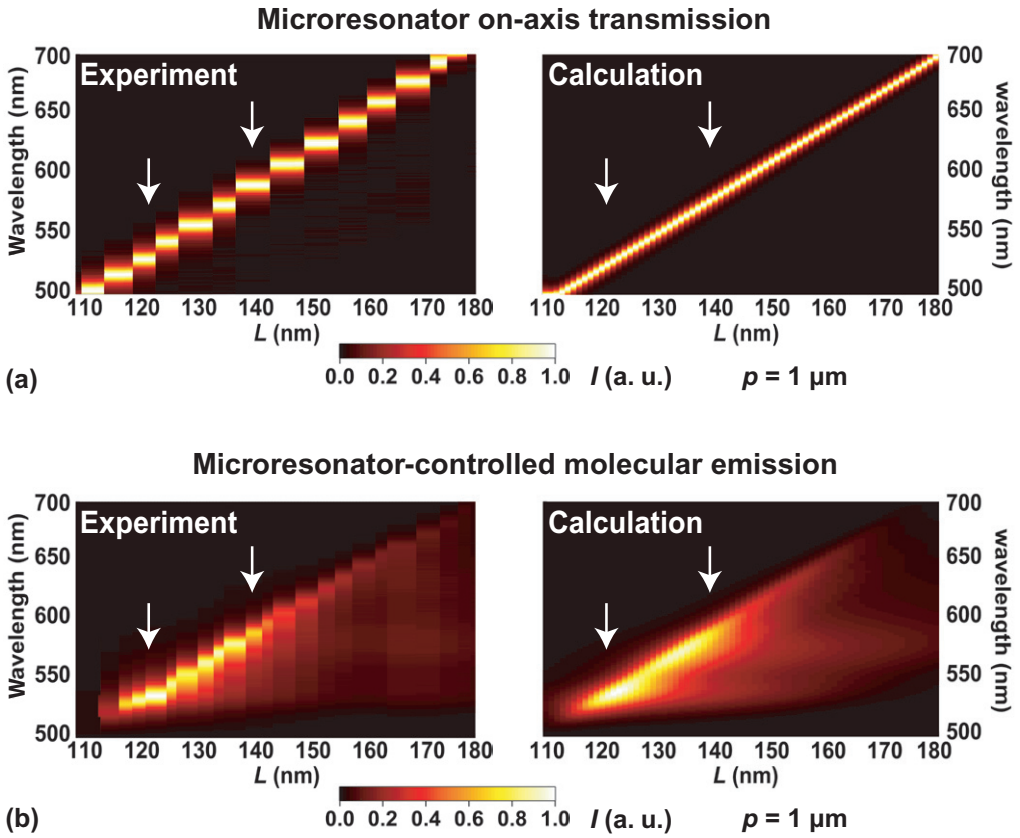

Figure 6. (a) Measured (left) and calculated (right) on-axis transmission spectra of the microresonator as a function of the mirror spacing L. (b) Measured (left) and calculated (right) spectral distribution of the fluorescence emission of ensembles of PI molecules as function of L. Representative cross sections taken at $L = 120$ nm and $L = 140$ nm (indicated by white arrows) are shown in figure 7.

molecular SpE rate in free (non-confined) space. The maximum Γ_{SpE} occurs at $L = 150$ nm for both molecular ensembles and single molecules. In contrast, we have observed the maximum of the integrated microresonator-controlled fluorescence intensity for L around 130 nm (see figure 3(f)). This difference ΔL is associated with imperfect optical confinement and can only be further decreased by increasing the mirror reflectivities $R_{1,2}$ (see also chapter 5 of [32]).

4.2. Microresonator-controlled spectral line shape of transmission and emission

In figure 6(a), we show series of measured and calculated on-axis transmission spectra of the microresonator as a function of the mirror spacing confirming the linear relation between $L(x)$ and $\lambda(x)$ throughout the $\lambda/2$-regime ($m = 1$ and $\vartheta = 0$ in (1)). In figures 7(a) and (b), we compare experimental and theoretical spectra for the two specific mirror spacings $L = 120$ nm and $L = 140$ nm. For the calculation of the on-axis transmission spectra, we assumed a parallel polarization of the incident optical field with respect to the plane of the metal mirrors $M_{1,2}$.

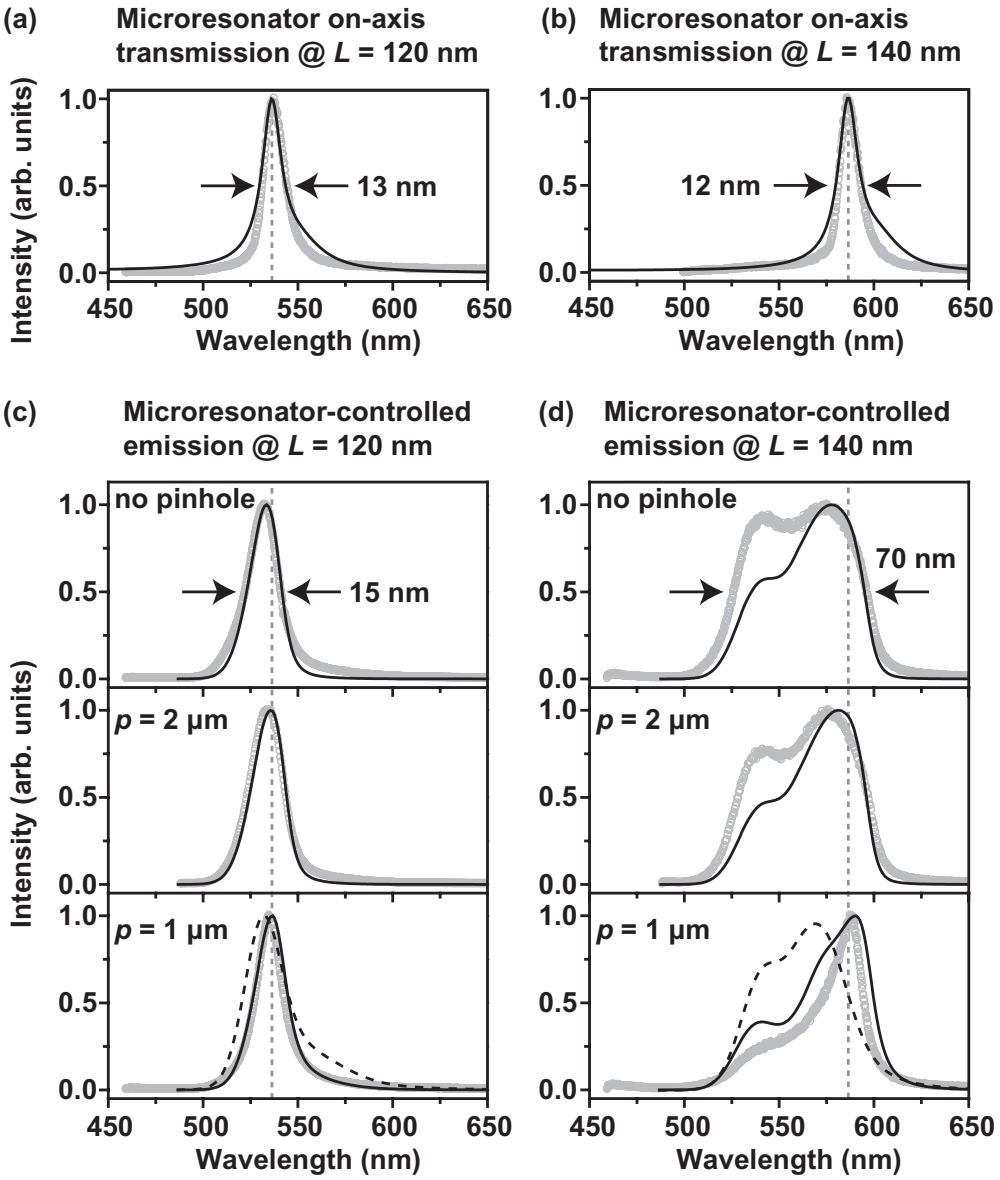

Figure 7. Measured (gray) and calculated (black) on-axis transmission spectra (a) and (b), and microresonator-controlled fluorescence spectra (c) and (d) for $L = 120\,\text{nm}$ and $L = 140\,\text{nm}$, respectively. The vertical dashed lines highlight the respective local maximum transmission wavelengths $\lambda(x)$ and the arrows indicate the spectral full-width-at-half-maximum. For $L = 120\,\text{nm}$, the spectral shape is insensitive to reduction of the effective observation area p on the microresonator surface by a confocal pinhole. For $L = 140\,\text{nm}$, the influence of reducing the effective observation diameter p is clearly visible. Calculated microresonator-controlled fluorescence spectra based on the (unmodified) SpE rate of PI molecules in free (non-confined) space are shown as dashed lines in the lower panels.

While we find good agreement for peak wavelengths as well as spectral widths of measured and calculated transmission spectra, the line shapes of the calculated intensity distributions exhibit a weak shoulder on the red side resulting in a slight spectral asymmetry with respect to the center wavelength $\lambda(x)$ that is more pronounced than in the measured spectra.

Spectrally resolved microresonator-controlled fluorescence scans are shown in figure 6(b). Like for the on-axis transmission spectra, the bright diagonal stripe reflects the proportional relation between L and λ. In the present case, however, the spectral distribution broadens significantly with increasing L due to increasing off-axis contributions and the calculations based on the microresonator-controlled SpE rate (see figure 5) match the experimental results.

In figures 7(c) and (d), we compare microresonator-controlled fluorescence spectra taken from figure 6(b) at $L = 120\,\text{nm}$ and 140 nm, respectively. For $L = 120\,\text{nm}$, we observe a spectrally narrow and nearly symmetric fluorescence band (see figure 7(c)) that is in excellent agreement with the intensity distribution calculated using (26) and very similar to the corresponding local on-axis transmission spectrum (see figure 7(a)). For this specific mirror spacing, the spectral shape of the microresonator-controlled fluorescence is insensitive to variations of the effective observation diameter p on the microresonator surface since radiation is predominantly emitted in forward direction ($\vartheta = 0$). Note, that the molecular emission spectra shown in figure 7(c) have been acquired with a full collection angle $2\vartheta_{\text{max}} = 120^{\circ}$ without any additional spectral or angular filtering. For comparison, we show the microresonator-controlled fluorescence line shape that has been calculated by assuming the constant molecular fluorescence rate $\Gamma_{\text{SpE},0}$ in free (non-confined) space and we observe a slight mismatch of both spectral position and line shape.

The increased spectral line width for $L = 140\,\text{nm}$ (see figure 7(d)) originates from off-axis emission on the blue side of the spectrum. While for on-axis emission ($\vartheta = 0$) the number of cavity roundtrips is only limited by the absorption losses in the silver mirrors, the off-axis emission ($\vartheta > 0$) walk off the observation area p within a small number of internal reflections. Apparently, the detection of this off-axis emission can be suppressed by stepwise reducing the effective observation diameter, i.e. by spatial filtering the microresonator-controlled fluorescence. For $L = 140\,\text{nm}$, we observe that the microresonator-controlled fluorescence line shape that has been calculated based on the unmodulated free-space rate $\Gamma_{\text{SpE},0}$ shows significant deviations from the measured spectral distribution.

As a key result, the microresonator-controlled fluorescence rate $\Gamma_{\text{SpE}}(L)$ observed for broadband emitting PI molecules (see figure 5) determines the microresonator-controlled fluorescence spectrum as a function of the mirror spacing as given by (26) and the measured spectral intensity distribution can only be quantified if the occurring rate modifications are accounted for properly.

4.3. Coupling ratio and spectral ratio

In figure 8, we show the coupling ratio β for microresonator-controlled PI fluorescence that has been calculated based on (14). The curve displays the ratio between molecular SpE into the local on-axis (forward) cavity mode and the total emission as a function of the mirror spacing assuming a PI molecule to be located in the center of the microresonator and oriented parallel to the resonator mirrors. We assumed that the forward mode is spectrally characterized by $\Delta\lambda = \lambda(x) \pm 6.5\,\text{nm}$, i.e. the full-width-at-half-maximum-value of the measured and calculated local

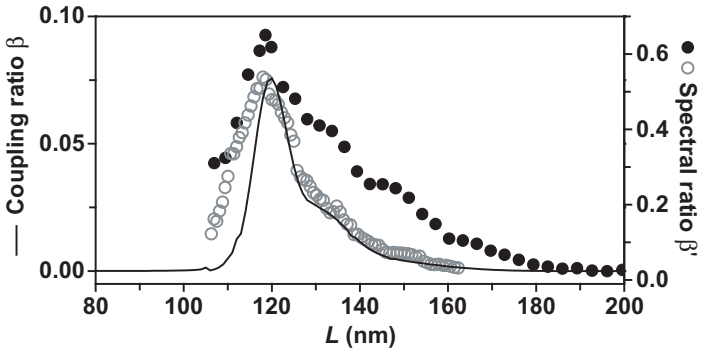

Figure 8. Calculated coupling ratio β (line) of microresonator-controlled PI-fluorescence emission to the on-axis cavity resonance as a function of mirror spacing L. Experimental spectral ratios β' as determined from the overlap of the local on-axis transmission spectrum and the corresponding microresonator-controlled emission spectrum as a function of the mirror spacing L. The underlying fluorescence spectra have been acquired with a confocal pinhole ($p = 1\,\mu$m, black circles) and without confocal pinhole (gray rings) in the detection path, respectively.

on-axis transmission spectrum with maximum transmission wavelength $\lambda(x)$ (see figures 7(a) and (b)). We modeled the corresponding angular range $\Delta\vartheta$ associated with the forward mode as a function of L based on the definition reported in [44] by accounting for the actual microresonator parameters. The resulting ratio β peaks for $L = 120$ nm, close to the mirror spacing where we also observe the maximum integrated intensity (see figures 3(e) and (f)).

For comparison, we determined experimentally the spectral ratio β' (rings, circles in figure 8) from the overlap of the measured local on-axis transmission spectrum of the microresonator and the corresponding measured fluorescence spectrum for each L (see figure 7) and we observe a nearly quantitative agreement between the calculated curve and the experimental curves. The shoulder around $L = 130$ nm reflects the vibronic progression of the free-space fluorescence spectrum of PI (see figure 1(b)). As expected, β' has larger values than β because not all fluorescence produced in the structure can be recorded in the respective microresonator-controlled fluorescence spectra due to the limitations of the collection angle $\vartheta_{\max}$. Reducing the diameter of the effective observation area p on the microresonator by a confocal pinhole (spatial filter) reduces the detection efficiency for off-axis emission, equivalent to angular filtering by limiting ϑ (see section 3.3). As a result, β' increases due to the suppression of off-axis contributions in the corresponding microresonator-controlled fluorescence spectra. However, the L-value for maximum β' is not affected by spatial filtering and coincides with the mirror spacing for maximum β. The maximum of β' indicates the maximum spectral narrowing as well as the minimum angular divergence of the microresonator-controlled fluorescence of PI molecules.

4.4. Microresonator-controlled single molecule fluorescence spectra

In figure 9, we show microresonator-controlled single molecule fluorescence spectra for three representative mirror spacings that have been measured without a confocal pinhole in

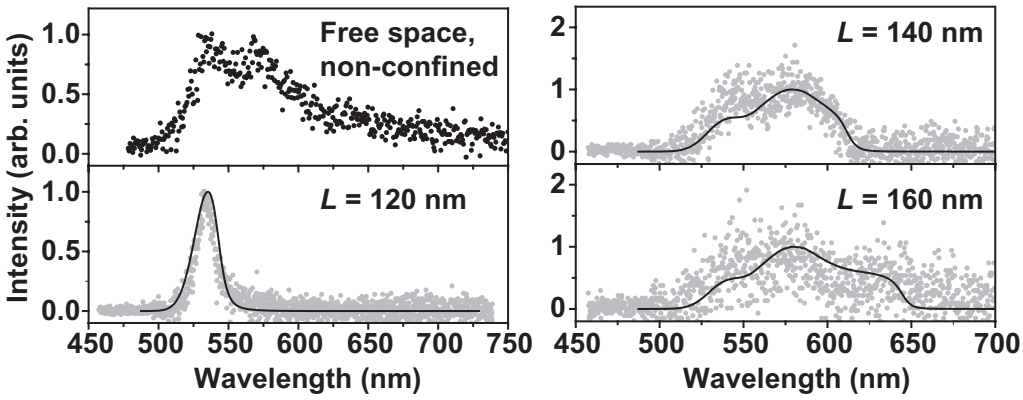

Figure 9. Measured (gray dots) and calculated (lines) microresonator-controlled single molecule fluorescence spectra for three different mirror spacings L. A free space single molecule fluorescence spectrum (black dots) is shown as a reference.

the detection path. As compared to the single molecule fluorescence spectrum measured in free space, we observe that the line width of the microresonator-controlled single molecule fluorescence spectrum measured for L around 120 nm is reduced up to six times [30]. In contrast to the microresonator-controlled single molecule fluorescence rate Γ_{SpE} (see figure 5), we find that the spectral shape of the measured single molecule fluorescence spectra is rather insensitive to the specific orientation and z-position of the molecular transition dipole: all measured spectra can be modeled satisfactorily using (26) by assuming in-plane dipole orientations (θ=0°) for the specific mirror spacing L. For increasing L, an increase of off-axis emissions leads to a spectral broadening in the microresonator-controlled single molecule fluorescence spectra. As a result, the signal-to-noise ratio in the spectra shown in figure 9 decreases with increasing mirror spacing: 5 for $L = 120$ nm, 2.5 for $L = 140$ nm and 1.5 for $L = 160$ nm. For larger L-values, the signal drops below the detection limit (see also figure 3(e)).

4.5. Higher orders of interference: fluorescence line shape and optical confinement

In the following, we investigate the influence of decreasing optical confinement on the spectral line shape of the microresonator-controlled broadband fluorescence. In figure 10(a), we compare on-axis transmission spectra and microresonator-controlled fluorescence spectra measured for six representative orders of interference m (see also figure 1(c)). We obtained the corresponding mirror spacings L using (1) and derived the experimental cavity-Q-values from Lorentzian fits to the on-axis cavity resonance at 530 nm after transformation into frequency space. For comparison, we estimate cavity-Q-values based on the calculated reflectivities $R_{1,2}$ of the silver mirrors $M_{1,2}$ following [45] by using

$$Q = \frac{\omega}{\Delta\omega} = \frac{2\pi (R_1 R_2)^{1/4}}{1 - \sqrt{R_1 R_2}} \cdot m \tag{28}$$

with R_1=0.71, R_2=0.91 and m varying from 1 to 20, or, in other words, from $\lambda/2$ to 10λ, and the results are shown in figure 10(b). The deviations between experimental and theoretical Q-values

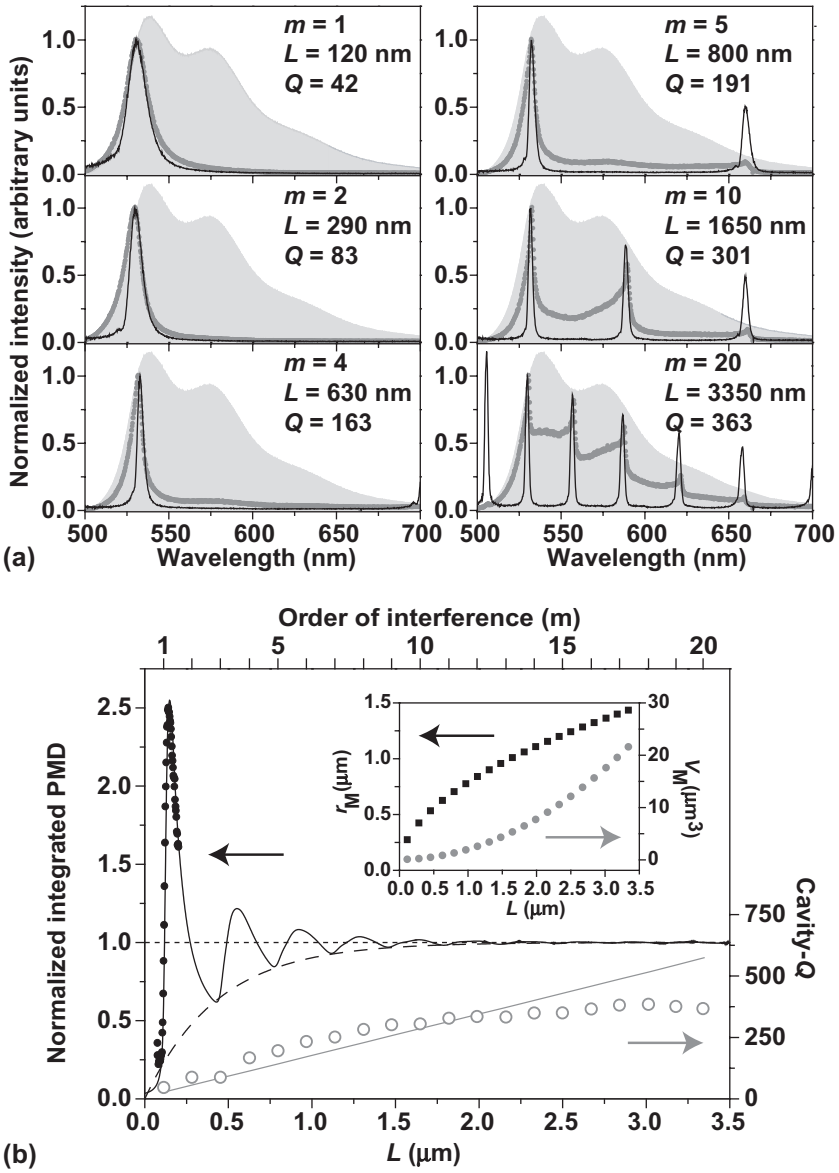

Figure 10. (a) Microresonator-controlled fluorescence spectra (gray dotted lines) and corresponding on-axis transmission spectra (black solid lines) measured for six representative orders of interference m. The measured free space fluorescence spectrum of PI molecules (light gray area) is shown as a reference in each panel. (b) Integrated and normalized PMD (experiment: circles, calculation: line, fit: dashed line) and cavity-Q of the microresonator (experiment: gray rings, calculation: gray line) as a function of the mirror spacing L. The PMD in free (non-confined) space is unity and indicated by the horizontal dashed line. (Inset) Calculated spatial mode radius r_M and mode volume V_M, respectively, of the longitudinal (on-axis) cavity mode at 530 nm as a function of L.

for smaller m-values indicate that the actual mirror reflectivities in the microresonator sample are slightly higher than the calculated R_i-values while the degression of the measured cavity-Q for larger m-values is caused by the increasing inclination $\alpha(L)$ between the microresonator mirrors $M_{1,2}$ (see also figure 1(a)).

For increasing m and, hence, L we observe the expected reduction of the spectral line width of the on-axis (forward) cavity resonance (see figure 10(a)). The associated increase of the cavity-Q is accompanied by a reduction of the free spectral range, i.e. the spectral spacing between successive on-axis cavity resonances, that becomes visible for $m = 5$. For $m = 1$ and $L = 120\,\text{nm}$, the spectral shape of the microresonator-controlled fluorescence samples the on-axis transmission spectrum and virtually all detected emission is extracted from the forward mode of the microresonator without the need for spectral or angular filtering (see also figures 7(a) and (c)). For increasing m, we observe stepwise the increasing deviations from the measured on-axis transmission spectra: while the microresonator-controlled fluorescence still reveals pronounced intensity maxima at the spectral positions of the on-axis cavity resonances, the overall spectral shape indicates decreasing optical confinement. For $m = 20$, the microresonator-controlled fluorescence line shape is already very similar to the fluorescence spectrum measured in free (non-confined) space.

Indeed, as shown in figure 10(b), the oscillations of the integrated and normalized PMD as seen by PI molecules in the center of the microresonator and oriented parallel to the resonator mirrors, i.e. $\text{PMD} = (\Gamma_{\text{SpE},0})^{-1} \int \Gamma_{\text{SpE},y}(\lambda, L)\,\text{d}\lambda$ based on (14), decay exponentially and a model fit to the minima of the PMD delivers $L_{1/e} = (431 \pm 6)\,\text{nm}$. In the first place, this decay is associated with the increasing mode volume V_{M} of the spatial modes between $M_{1,2}$ effectively realizing the optical confinement for the embedded molecules [36, 38, 44], [46]–[48]. We estimate the spatial mode radius r_{M} of the local forward mode at $\lambda(x) = 530\,\text{nm}$ as a function of the mirror spacing $L(x)$ following [46, 48] by using

$$r_{\text{M}} = \sqrt{\frac{\pi\lambda(x)L(x)(R_1R_2)^{1/4}}{8n_{\text{pol}}(1-\sqrt{R_1R_2})}}, \tag{29}$$

for $n_{\text{pol}} = 1.56$, $R_1 = 0.71$, $R_2 = 0.91$ and the results are shown in the inset of figure 10(b). We observe a rather smooth slope of V_{M} for small L that does not fit the rapid decay of the oscillations of the PMD as seen by the PI molecules. The reason is that the actual photonic mode volume also includes contributions from off-axis cavity modes effectively relaxing the optical confinement for the embedded molecular broadband-emitters. The PMD shown in figure 10(b) accounts for the (multi-spectral) coupling to these off-axis cavity modes.

5. Summary and conclusions

We have correlated the microresonator-controlled fluorescence line shape of broadband-emitting dye molecules with the modifications of the molecular SpE rate imposed by optical confinement down to the single molecule level. By tuning the mirror spacing of the microresonator throughout the $\lambda/2$-regime with nanometer-precision, we observe that the molecular SpE rate can be inhibited (enhanced) by a factor of 0.21 (2.5) with respect to the molecular SpE rate in free (non-confined) space. The microresonator-controlled fluorescence line shape and line width, respectively, are determined by these variations of the molecular SpE

rate. The fluorescence line width of molecular ensembles and single molecules can be reduced by up to one order of magnitude as compared to the original value in free space without the need for additional spectral, spatial or angular filtering. The optical confinement and the oscillation of the molecular SpE rate vanish for mirror spacings exceeding 500 nm while the cavity-Q, the spatial mode radius and the spatial mode volume of the microresonator increase monotonically. In consequence, the spectral line shape of the microresonator-controlled fluorescence converges towards the free-space spectrum. The results may impact research on and applications of broadband emitters and optical confinement in nano-optics and nano-photonics as well as ultra-sensitive (single molecule) chemical analysis and biosensing.

Acknowledgments

We thank G Schulte (Siegen University) for technical support and acknowledge financial support by the Deutsche Forschungsgemeinschaft DFG (Me 1600/6-1/2) and the Landesstiftung Baden-Württemberg. The scan images shown in figures 3(c) and (d) were processed using WSXM software [49].

References

[1] Yokoyama H and Ujihara K 1995 *Spontaneous Emission and Laser Oscillation in Microcavities* (Boca Raton, FL: CRC Press)
[2] Chang R K and Campillo A J 1996 *Optical Processes in Microcavities* (Singapore: World Scientific)
[3] Vahala K J 2003 Optical microcavities *Nature* **424** 839–46
[4] Benson T M, Boriskina S V, Sewell P, Vukovic A, Greedy S C and Nosich A I 2006 Micro-optical resonators for microlasers and integrated optoelectronics *Frontiers in Planar Lightwave Circuit Technology* vol 216 (Berlin: Springer) pp 39–70
[5] Kleppner D 1981 Inhibited spontaneous emission *Phys. Rev. Lett.* **47** 233–6
[6] Purcell E M 1946 Spontaneous emission probabilities at radio frequencies *Phys. Rev.* **69** 681
[7] Bennett A J, Unitt D C, See P, Shields A J, Atkinson P, Cooper K and Ritchie D A 2005 Microcavity single-photon-emitting diode *Appl. Phys. Lett.* **86** 181102
[8] Steiner M, Korlacki R, Hartschuh A and Meixner A J 2007 Highly efficient, tunable single photon source based on single molecules *Appl. Phys. Lett.* **90** 183122
[9] Steiner M, Qian H, Hartschuh A and Meixner A J 2007 Controlling nonequilibrium phonon populations in single-walled carbon nanotubes *Nano Lett.* **7** 2239–42
[10] Xia F, Steiner M, Lin Y-M and Avouris Ph 2008 A microcavity-controlled, current-driven, on-chip nanotube emitter at infrared wavelengths *Nat. Nanotechnol.* **3** 609–13
[11] Steiner M, Xia F, Qian H, Lin Y-M, Hartschuh A, Meixner A J and Avouris Ph 2008 Carbon nanotubes and optical confinement: controlling light emission in nanophotonic devices *Proc. SPIE* **7037** 703713
[12] Stefani F D, Vasilev K, Bocchio N, Stoyanova N and Kreitner M 2005 Surface-plasmon-mediated single-molecule fluorescence through a thin metallic film *Phys. Rev. Lett.* **94** 023005
[13] Buchler B C, Kalkbrenner T, Hettich C and Sandoghdar V 2005 Measuring the quantum efficiency of the optical emission of single radiating dipoles using a scanning mirror *Phys. Rev. Lett.* **95** 063003
[14] Anger P, Bharadwaj P and Novotny L 2006 Enhancement and quenching of single-molecule fluorescence *Phys. Rev. Lett.* **96** 113002
[15] Kühn S, Håkanson U, Rogobete L and Sandoghdar V 2006 Enhancement of single-molecule fluorescence using a gold nanoparticle as an optical nanoantenna *Phys. Rev. Lett.* **97** 017402
[16] Taminiau T H, Stefani F D, Segerink F B and van Hulst N F 2008 Optical antennas direct single-molecule emission *Nat. Photonics* **2** 234–7

[17] Rigneault H, Capoulade J, Dintinger J, Wenger J, Bonod N, Popov E, Ebbesen T W and Lenne P-F 2005 Enhancement of single-molecule fluorescence detection in subwavelength apertures *Phys. Rev. Lett.* **95** 117401
[18] Moerner W E 2004 Single-photon sources based on single molecules in solids *New J. Phys.* **6** 88
[19] Lounis B and Orrit M 2005 Single-photon sources *Rep. Prog. Phys.* **68** 1129–79
[20] Enderlein J 2000 Theoretical study of detection of a dipole emitter through an objective with high numerical aperture *Opt. Lett.* **25** 634–6
[21] Moerner W E and Fromm D P 2003 Methods of single-molecule fluorescence spectroscopy and microscopy *Rev. Sci. Instrum.* **74** 3597–619
[22] Kulzer F and Orrit M 2004 Single-molecule optics *Annu. Rev. Phys. Chem.* **55** 585–611
[23] Novotny L and Hecht B 2006 *Principles of Nano-Optics* (Cambridge: Cambridge University Press)
[24] De Martini F, Di Giuseppe G and Marrocco M 1996 Single-mode generation of quantum photon states by excited single molecules in a microcavity trap *Phys. Rev. Lett.* **76** 900–3
[25] Kitson S C, Jonsson P, Rarity J G and Tapster P R 1998 Intensity fluctuation spectroscopy of small numbers of dye molecules in a microcavity *Phys. Rev.* A **58** 620–7
[26] Rigneault H, Monneret S and Westbrook C I 1998 Resonant focusing in a planar microcavity *J. Opt. Soc. Am.* B **15** 2712–5
[27] Khoptyar D, Gutbrod R, Chizhik A, Enderlein J, Schleifenbaum F, Steiner M and Meixner A J 2008 Tight focusing of laser beams in a λ/2-microcavity *Opt. Express* **16** 9907–17
[28] Becker H, Burns S E, Tessler N and Friend R H 1997 Role of optical properties of metallic mirrors in microcavity structures *J. Appl. Phys.* **81** 2825–9
[29] Worthing P T, Wasey J A E and Barnes W L 2001 Rate and efficiency of spontaneous emission in metal-clad microcavities *J. Appl. Phys.* **89** 615–25
[30] Steiner M, Schleifenbaum F, Stupperich C, Failla A V, Hartschuh A and Meixner A J 2005 Microcavity-controlled single-molecule fluorescence *ChemPhysChem* **6** 2190–6
[31] Steiner M, Schleifenbaum F, Stupperich C, Failla A V, Hartschuh A and Meixner A. J 2006 A new microcavity design for single molecule detection *J. Lumin.* **119-120** 167–72
[32] Steiner M 2006 Control of molecular spontaneous emission in an optical λ/2-microresonator *PhD Thesis* Siegen University
[33] Born M and Wolf E 1980 *Principles of Optics* 6th edn (Oxford: Pergamon Press)
[34] De Martini F, Marrocco M, Mataloni P, Crescentini L and Loudon R 1991 Spontaneous emission in the optical microscopic cavity *Phys. Rev.* A **43** 2480–97
[35] Fermi E 1932 Quantum theory of radiation *Rev. Mod. Phys.* **4** 87–132
[36] Steiner M, Hartschuh A, Schleifenbaum F and Meixner A J 2008 Coupled molecular excited states form unstable spatial modes in an optical λ/2-microresonator *J. Lumin.* **128** 803–6
[37] De Martini F and Jacobovitz G R 1988 Anomalous spontaneous-stimulated-decay phase transition and zero-threshold laser action in a microscopic cavity *Phys. Rev. Lett.* **60** 1711–4
[38] De Martini F, Marrocco M and Murra D 1990 Transverse quantum correlations in the active microscopic cavity *Phys. Rev. Lett.* **65** 1853–6
[39] Agarwal G S and Dutta Gupta S 1998 Microcavity-induced modification of the dipole–dipole interaction *Phys. Rev.* A **57** 667–70
[40] Hopmeier M, Guss W, Deussen M, Göbel E O and Mahrt R F 1999 Enhanced dipole–dipole interaction in a polymer microcavity *Phys. Rev. Lett.* **82** 4118–21
[41] Andrew P and Barnes W L 2000 Förster energy transfer in an optical microcavity *Science* **290** 785–8
[42] de Dood M J A, Knoester J, Tip A and Polman A 2005 Förster transfer and the local optical density of states in erbium-doped silica *Phys. Rev.* B **71** 115102
[43] Temnov V V and Woggon U 2005 Superradiance and subradiance in an inhomogeneously broadened ensemble of two-level systems coupled to a low-*Q* cavity *Phys. Rev. Lett.* **95** 243602

[44] Björk G, Heitmann H and Yamamoto Y 1993 Spontaneous-emission coupling factor and mode characteristics of planar dielectric microcavity lasers *Phys. Rev.* A **47** 4451–63
[45] Lipson S G, Lipson H S and Tannhauser D S 1997 *Optik* (Berlin: Springer)
[46] Ujihara K 1991 Spontaneous emission and the concept of effective area in a very short optical cavity with plane-parallel dielectric mirrors *Japan. J. Appl. Phys.* **30** L901–3
[47] De Martini F, Cairo F, Mataloni P and Verzegnassi F 1992 Thresholdless microlaser *Phys. Rev.* A **46** 4220–33
[48] Kai K, Oh-Hara C, Inoue H, Yamanaka T and Ujihara K 2002 Measurement of the characteristic transverse mode radius of a planar microcavity laser *Japan. J. Appl. Phys.* **41** 7398–9
[49] Horcas I, Fernández R, Gómez-Rodríguez J M, Colchero J, Gómez-Herrero J and Baro A M 2007 WSXM: a software for scanning probe microscopy and a tool for nanotechnology *Rev. Sci. Instrum.* **78** 013705